

Characterization and modelling of bisphenol-a type epoxy polymer over a wide range of rates and temperatures

Huanming Chen, Peihao Song, Thomas Commins, Aaron Graham, Akash R. Trivedi, Clive R. Siviour^{*}

Solid Mechanics and Materials Engineering, Department of Engineering Science, University of Oxford, Oxford, OX1 3PJ, United Kingdom

ARTICLE INFO

Keywords:

Epoxy
Dynamic mechanical analysis
High-rate
Temperature-strain-rate equivalence
Three-network (TN) model

ABSTRACT

Epoxy resins are employed in many engineering applications in which mechanical properties at different strain rates and temperatures must be quantified for effective use. It is known that these properties are related through the principle of time-temperature equivalence. In this paper, the application of this equivalence is explored in detail, at both small and large strains, and used as part of a strategy for calibrating a constitutive model that can reproduce the stress-strain behaviour in different mechanical conditions. In order to achieve this, quasi-static compression experiments were performed at temperatures from -40 to $+40$ °C in a screw-driven load frame; room temperature rate dependent experiments were performed from 0.0005 to 6300 s⁻¹ using a screw-driven load frame, hydraulic compression system and Split Hopkinson Pressure Bar apparatus. Dynamic mechanical analysis and differential scanning calorimetry were also performed. A three-network (TN) polymer model was fit to the mechanical behaviour up to a strain of 0.5 . This model, combined with time-temperature based mappings gave a good understanding of the thermomechanical behaviour of the material, and also demonstrates an approach that can be used for a wide range of polymers.

1. Introduction

Epoxy resins are frequently used in engineering products that experience impact loading, so it is important to understand their behaviour under high strain rate deformation. It is well known that as the loading rate increases, polymers exhibit an increase in both modulus and yield stress, and that in many materials a 'bilinear' dependence on log strain rate is observed above ~ 100 s⁻¹, because of restrictions in mobility of the β relaxations [1,2].

In addition to the strain rate, the temperature has a significant effect on mechanical properties, with the polymer becoming stiffer and stronger (higher yield stress) as the temperature is reduced [1,3–6]. It is observed that this mirrors the rate dependence: the polymer exhibits synchronous property changes of increased moduli, yield stress and post-yield stress at either low temperatures or high rates. At high temperature or low strain rates only the α -transition (glass transition) plays a role in the mechanical properties, whilst at low temperature or high strain rates, the β -transition contributes to the overall behaviour. Jordan et al. [7], Rio et al. [8] and Tamrakar et al. [9] examined epoxy material at high strain rates (up to 10^4 s⁻¹) and low temperatures, and found that

the β -transition (strictly, the restriction of β motions) led to increases in peak stress at rates above 10^2 s⁻¹. Tian et al. [10] reported rate sensitivity and bilinear behaviour in epoxy-nanocomposites.

The time-temperature superposition (TTS) principle is often used to describe the equivalence of a polymer's mechanical properties observed from time and temperature dependent experiments; these may be large strain compression or tension tests, or small strain tests such as dynamic mechanical analysis (DMA) [11]. A simple procedure is to map the dependence of the yield stress on temperature to the dependence on strain rate using an empirical formula [1], using a reference strain rate ($\dot{\epsilon}_0$) and reference temperature (T_0) as experimental constants, as well as an experimentally determined mapping constant, here expressed as D :

$$T - T_0 = D \left(\frac{\log \dot{\epsilon}_0}{\log \dot{\epsilon}} \right). \quad (1)$$

The parameter D relates the strain rate and temperature sensitivities during deformation of the polymer, in units of temperature per decade of strain rate. Siviour et al. [1] first mapped the peak stress of polycarbonate (PC) with variation of temperature and strain rate using one single constant. Williamson et al. [12] used the same principle to

^{*} Corresponding author.

E-mail address: clive.siviour@eng.ox.ac.uk (C.R. Siviour).

<https://doi.org/10.1016/j.polymer.2022.124860>

Received 5 April 2022; Accepted 13 April 2022

Available online 18 April 2022

0032-3861/© 2022 The Authors. Published by Elsevier Ltd. This is an open access article under the CC BY license (<http://creativecommons.org/licenses/by/4.0/>).

graphically map varying temperature data onto varying strain rate data in polymer-bonded composites. Jordan et al. [13] examined temperature-strain-rate equivalence in PTFE with good agreement. Kendall et al. [14] have taken this principle further by simulating not only in increased yield stress at higher rates, but also the effects of adiabatic heating: during high strain rate loading the thermodynamic condition changes from isothermal to adiabatic, which can cause temperature rises and therefore thermal softening in the materials during loading [15–17]. Furmanski et al. [18] extended the equivalence relation to a continuous stress-strain curve with large strain for the estimation of isothermal deformation states. Other polymers, including PTFE, HDPE, PE, HTPB, etc, also have been widely examined using this mapping theorem [19, 20]. However, it is observed that the time-temperature sensitivity of each relaxation in the polymer itself can be different, and one single linear mapping coefficient might only work within a finite region. Deviations and matching errors might emerge at high rates [3,14,18], this is understood to be the contribution of the β -transition.

Several models have been developed to describe large strain time-temperature equivalence in polymers [21,22], often using the Ree–Eyring approach and multiple processes of rate-activation [23], and these have also been applied to epoxies. Tamrakar et al. [9] employed the Ree–Eyring model comprising both α and β relaxations to predict the yield stress over a wide range of strain rates in DER 353 epoxy resin. Jordan et al. [7] employed the Mulliken–Boyce model [24], which also has separate α and β processes, to predict high-rate behaviour of EPON 826 epoxy. Sorini et al. [25] proposed a viscoplastic constitutive model with hydrostatic influence and a plastic potential function to characterise representative epoxy over a range of strain rates, temperatures, and loading cases. Recently, the direct observations of atomic properties and use of molecular dynamics (MD) simulations [26] also allowed systematic estimates of polymer mechanical properties at extremely high strain rates of 10^7 – 10^9 s^{−1} [27]. However, these atomic level predictions may have less practical relevance to engineering applications of polymeric products.

In the work presented in this paper, a three-network (TN) model [28] is adopted. The model consists of three parallel chains comprising two separate energy activation mechanisms and a large strain response controlled by entropic resistance. The TN model has frequently been used for polymeric materials to describe strain-rate and temperature dependent behaviour up to large strains [29–35].

In this research, an epoxy polymer was first characterised *via* differential scanning calorimetry (DSC) and dynamic mechanical analysis (DMA). Then, the large strain mechanical properties were investigated at temperatures from −40 to 40 °C at a strain rate of 0.01 s^{−1} and strain rates from 0.0005 to 6300 s^{−1} at room temperature. The empirical stress-strain data from these experiments were explored using the principle of time-temperature equivalence to produce an integrated mapping involving data from both DMA experiments and compression tests. Finally, the three-network (TN) model [36] was adopted to

reproduce the full range of stress-strain behaviour using parameters fitted to the experimental data. In summary, this paper presented a comprehensive study of the thermo-mechanical properties of an epoxy polymer.

2. Material & experiments

2.1. Epoxy polymer and specimen design

A transparent epoxy polymer (MinistryofCraft® Ltd, UK) was prepared by mixing resin and hardener in a standard ratio of 1:1 by volume. The resin includes Bisphenol A diglycidyl ether, Poly[(phenyl glycidyl ether)-co-formaldehyde] and Benzyl alcohol solvent; the hardener contains PPG-70 Bis-(2-Aminopropyl) ether [37] (Safety Data Sheets in Data Availability). A schematic diagram showing the end epoxy product is given in Fig. 1. To produce the solid epoxy, resin and hardener solvents were mixed at room temperature, stirred for 10 min, then degassed for another 15 min before being poured into a mould. The curing temperature was set at 45 °C and the resin was cured for 6 h. Cylindrical compression specimens were cut from the sheet with dimensions of 6 × 5 mm for quasi-static experiments, and 3 × 2.5 mm for split-Hopkinson bar tests at higher rates. A small number of tension experiments were performed using a standard specimen meeting ISO-527-Type1BA, with a gauge length of 25 mm, width of 5 mm and thickness of 2 mm was used.

2.2. Experimental methods

The small-strain thermomechanical properties were characterised *via* dynamic mechanical analysis (DMA) experiments, on a DMA TA Q800 machine in single-cantilever configuration. A beam-shape specimen (dimension 37.5 × 8.04 × 3.3 mm) was clamped to produce a gauge length of 17.31 mm and tested under cyclic deformation using isothermal frequency sweeps at a series of increasing temperatures. The machine reports complex modulus (E' and E''), loss tangent ($\tan \delta$), stress, temperature, and frequency; the first four are calculated from the amplitude and phase of the applied displacement and resultant force. Isothermal frequency sweeps at 0.1, 0.5, 1, 2.5 and 10 Hz were performed at 2 °C intervals from −110 °C to 90 °C. The displacement amplitude was set as 0.1% strain. From the outputs above, the moduli against loading frequency at each temperature can be used to produce a master curve of frequency dependence from which the storage modulus can be obtained, using the principle of time-temperature superposition.

Differential scanning calorimetry (DSC) was used to examine the thermal properties of the liquid resin, hardener agent and cured solid epoxy. The objective was to compare the thermal transitions in DSC to the DMA measurements. A small amount of liquid resin (~17.42 mg), hardener agent (~18.21 mg) and solid epoxy bulk (~7.45 mg) were prepared and sealed into aluminium pan containers. Each specimen was first allowed to reach thermal equilibrium at −80 °C, then heated at 5 °C

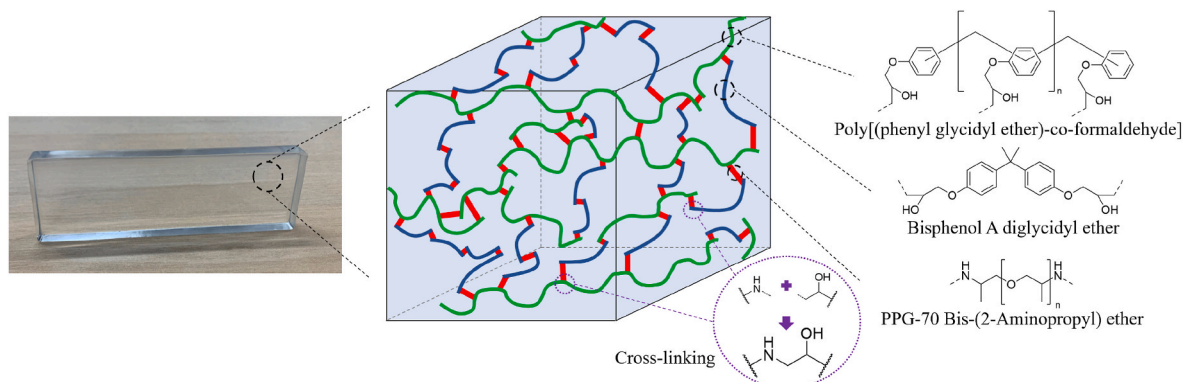


Fig. 1. Schematics of cross-linked epoxy resin.

min^{-1} up to $100\text{ }^{\circ}\text{C}$. The temperature was returned to $-80\text{ }^{\circ}\text{C}$ with $5\text{ }^{\circ}\text{C min}^{-1}$ cooling rate then a second heating loop started. The heat flow per unit mass (W g^{-1}) was recorded. The heat capacities ($\text{J kg}^{-1}\text{ K}^{-1}$) could then be determined.

Low-rate compression experiments were performed in a screw-driven Instron 5900 machine from 0.0005 to 0.5 s^{-1} . Grease lubrication was smeared on the contact surfaces to avoid friction. The crosshead moved under a ‘true strain rate’ control, using strain measurements from a contacting extensometer attached to the loading platens close to the specimen. A load-cell attached to the crosshead records the force. For experiments at low temperature an environmental chamber with liquid nitrogen cooling system was used. The tensile experiments were also performed in this machine, but here at a constant loading rate. A high-resolution camera (PointGrey) was used, spaced about 1 m from the sample with a 60 mm lens (Nikon), to take photographs at a frame rate of 5 fps . All photographs have a standard dimension of 512×2048 pixels, representing actual frame dimension of $16.2 \times 64.8\text{ mm}$. All images were analysed using commercial digital image correlation DIC software (MatchID®): the target frame of measurement on the tensile sample was 80×780 pixels, the subset size was 23 pixels, and step size 8 pixels. A virtual strain gauge of 700 pixels and logarithmic strain calculation were used to determine the instant true strain evolution. The true stress was again determined from the load cell records. One representative tensile test with DIC analysis is shown in Fig. SI-1, SI.

Intermediate strain rate experiments ($2, 12, 25\text{ s}^{-1}$) were executed in a servo-hydraulic testing machine, Fig. 2a. The attached LVDTs were used to record the displacement history. The force was measured using a calibrated load cell. For high rate experiments, the split Hopkinson pressure bar (SHPB) was employed [6]. The conventional SHPB apparatus, Fig. 2b, includes a striker, incident bar, and transmission bar. The striker is fired propelled by compressed air, impacting the incident bar and created an ‘incident’ stress wave travelling along the bar towards the specimen. At the bar-specimen interface, the reflected wave and transmitted wave are generated and move in opposite direction. The forces induced in the incident, reflected and transmitted pulses are measured by strain gauges attached to the incident and transmission bars. The initial cross-sectional area and length of the specimen are used to calculate the dynamic stress, strain, and strain rate using one-dimensional wave propagation theory. The stress and strain amplitude of the incident pulse is decided by the striker velocity and the stress wave speed in the striker.

3. Constitutive material model

The material response characterised in this paper can be captured using a simplified three-network representation [28] based on the Bergstrom-Boyce model [36,38]. The three-network model consists of three parts, or molecular networks, acting in parallel, Fig. 3. In this model, the viscoelastic and viscoplastic response are captured using two separated activation mechanisms, with a third network representing the large strain entropic response. In this paper, the very large strain response ($>1\text{ } \epsilon$) is not explored, thereby only network-A and network-B were needed to characterise the intrinsic material properties up to true strains of 0.5 . The detailed model description is given in Ref. [28], but for convenience an overview is given in the supplementary information

to this paper.

In order to fit the model, the required material parameters were calibrated with a software tool [39] MCalibration® and PolymerFEM® which extracted parameters by simultaneously using measured compression data from different temperature and rates.

4. Results and discussion

4.1. Thermodynamic analysis

The storage and loss moduli of the epoxy were measured using dynamic mechanical analysis (DMA); data are shown in Fig. 4. The storage modulus revealed a distinct glass transition, or α -transition, located around $27\text{ }^{\circ}\text{C}$ ($\sim 300\text{ K}$); the associated loss modulus peaks occurred at temperatures between $20\text{ }^{\circ}\text{C}$ ($\sim 293\text{ K}$) and $30\text{ }^{\circ}\text{C}$ ($\sim 303\text{ K}$) at the different frequencies. A second transition with less intensity appeared between $-51\text{ }^{\circ}\text{C}$ ($\sim 222\text{ K}$) and $-26\text{ }^{\circ}\text{C}$ ($\sim 247\text{ K}$) in the loss moduli. Although this transition is not immediately visible in the storage modulus data, it is observed in the derivative of this value, Fig. 4b, and also in the loss tangent data in Fig. 4c.

The transition temperatures (measured as the peaks of the loss modulus and loss tangent) are plotted against frequency Fig. 4d. This allows the temperature-frequency equivalence to be found: shift factors of 5.5 K per decade frequency for the glass transition and 15 K per decade frequency for the secondary transition. It is noted that for the same frequency increase, the shift to higher temperatures is larger for the secondary transition than for the glass transition. This information, which is consistent with other studies [24], will be used to interpret the experimental results in the next chapter.

The principle of time-temperature superposition (TTS) was implemented to produce a continuous ‘master curve’, shown in Fig. 5a. This was obtained by overlapping isotherms with their neighbours until a smooth, continuous curve was produced. As part of this process, each individual frequency plot is given its own shift to overlap its neighbour. The plot of shift factors obtained, Fig. 5b, indicated a glass transition temperature of approximately $38\text{ }^{\circ}\text{C}$ ($\sim 311\text{ K}$). A well-known function, the Williams–Landel–Ferry (WLF) equation [40] can be used to describe the temperature dependence of the factors around the glass transition:

$$\Delta \log(a_T) = \frac{C_1(T - T_g)}{C_2 + T - T_g}, \quad (8)$$

where T_g is the glass transition temperature and C_1 and C_2 are two fitting parameters.

The master curve can be modelled using a generalized Maxwell model and described using a Prony series [41], such that the storage modulus as a function of frequency, ω , can be described as

$$E'(\omega) = E_0 + \sum_{i=1}^n E_i \frac{\tau_i^2 \omega^2}{1 + \tau_i^2 \omega^2}, \quad (9)$$

where E_0 is a long-term modulus, and E_i is the modulus of a Maxwell branch of relaxation time τ_i . The equation is able to reproduce the continuous master curve describing storage moduli against frequency when an appropriate number of terms is used: 56 in this paper, listed in the SI.

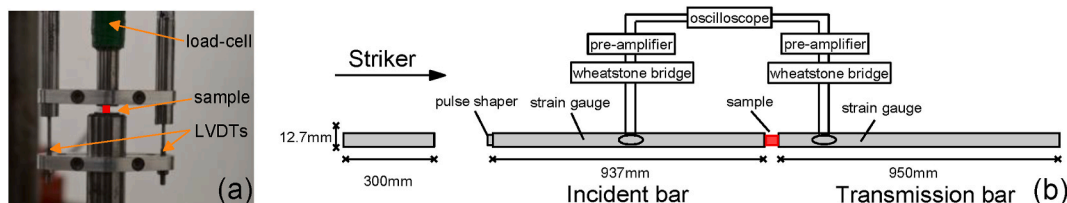


Fig. 2. (a) Image of the of hydraulic compressor used for medium rate experiments, and (b) schematic diagram of the SHPB apparatus used for high rate experiments.

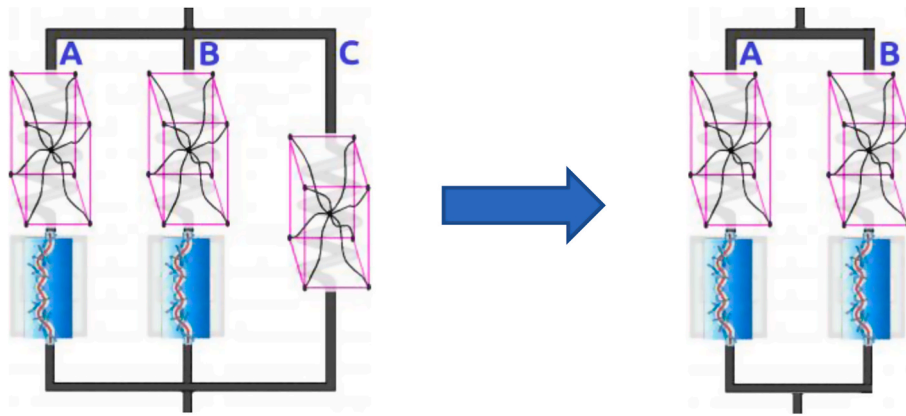


Fig. 3. Representation of the simplified constitutive model from three-network model [28].

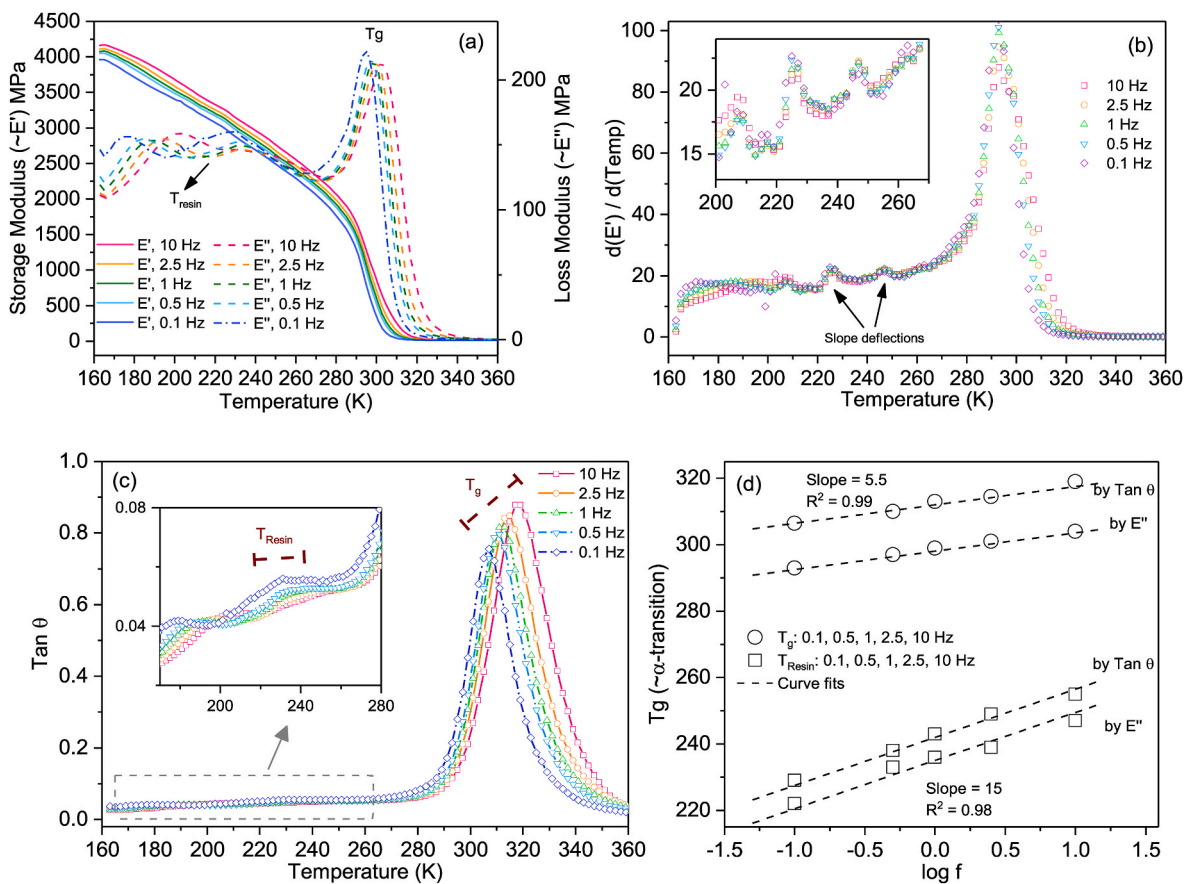


Fig. 4. DMA results of epoxy material at 0.1, 0.5, 1, 2.5 and 10 Hz: (a) storage and loss moduli; (b) differential coefficient of storage modulus to temperature; (c) loss tangent and (d) shift factors of temperature to per decade frequency at observed glass transition and secondary transition. Note that although these data are shown as functions of temperature, they were obtained as isothermal frequency sweeps.

Fig. 6a presents DSC data for the liquid resin and hardener agent, whilst data for the cured epoxy are shown in Fig. 6b. The resin shows a noticeable transition around -33°C ($\sim 240\text{ K}$); the hardener has a lower transition around -58°C ($\sim 215\text{ K}$). These are consistent with the low order transitions seen in the DMA and indicate that the transitions in the DMA are associated with these molecules within the epoxy structure. The solid epoxy has a glass transition temperature around temperature 38°C ($\sim 311\text{ K}$), and a weak transition at low temperature -18°C ($\sim 255\text{ K}$). These values are consistent with the DMA data.

Some interesting features are observed when comparing heat flow in thermal loops: the hardener agent shows a small feature around 57°C

($\sim 330\text{ K}$) in the first heating loop which is not present the second time: this might be a result of evaporation causing the mass to change. In the solid epoxy, the specimen shows the thermal effects of relaxation of local residual stresses in the material as it goes through the glass transition the first time, but not the second.

4.2. Large strain mechanical properties

The uniaxial compression experiments were first conducted on epoxy polymer at room temperature, $20 \pm 1^\circ\text{C}$ ($293 \pm 1\text{ K}$), across a range of strain rates from 5×10^{-4} to 0.5 s^{-1} . Stress-strain curves from the full

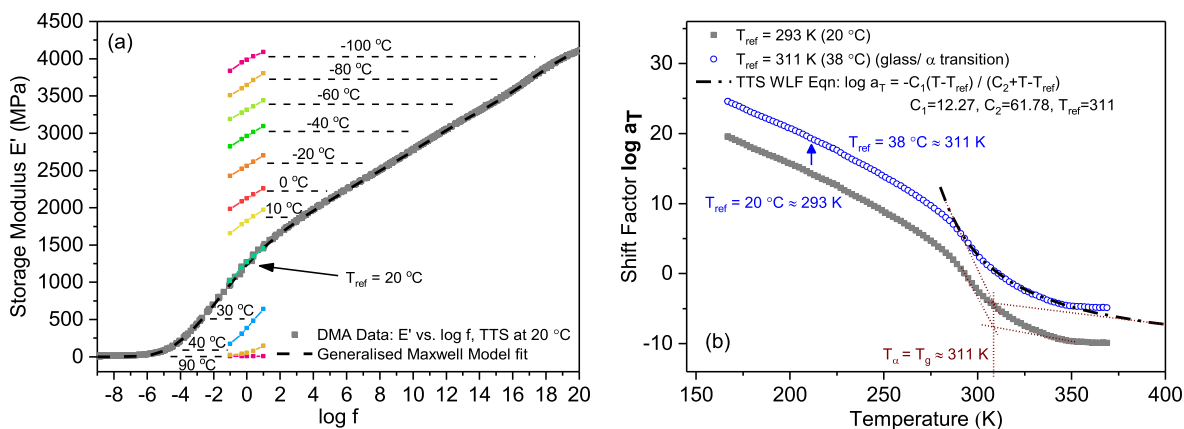


Fig. 5. The principle of TTS applied to DMA data: (a) Master curve and generalized Maxwell model fit; (b) Plot of shift factors fitted with WLF equation and the glass transition temperature identified. WLF equation evaluated at $T_g = 311$ K with parameters $C_1 = 12.27$, $C_2 = 61.78$ K.

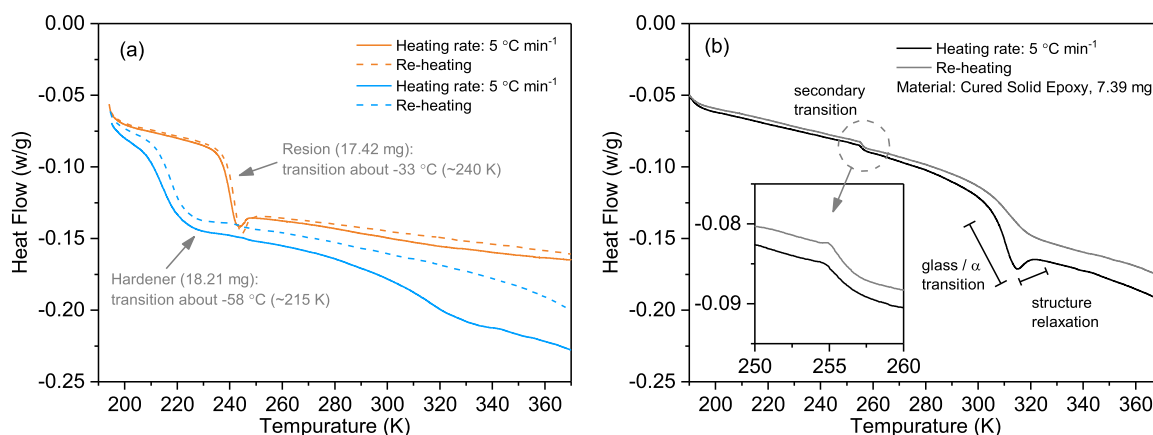


Fig. 6. DSC empirical data for liquid resin and hardener agent, (a), and cured solid epoxy (b).

range of rate- and temperature-dependent experiments are presented in Fig. 7. For strain rates up to 0.5 s^{-1} , three experiments were performed and an average stress-strain curve calculated. For higher strain rates, a representative curve is chosen. The full set of high rate experimental data are shown in Fig. SI-2. Fig. 8 shows the consistency of stiffnesses measured in these experiments to those expected from the viscoelastic model.

The rate and temperature dependence of the yield stress is shown in Fig. 9, which describes a typical 'bilinear' rate dependence, with an increase in gradient above $\log(\dot{\epsilon}) = 2.5$. The temperature dependence is, however, almost linear. In order to approximately map the rate and

temperature dependence onto each other the method described above (Eq (1)) was used, but with two different values of D representing the region dominated by the movement of the glass transition, for which $D = 5.5$ K per decade, and that dominated by the movement of the β -transition, for which $D = 15$ K per decade. These values were obtained from the DMA data in Fig. 4, and the boundary between the two regions was chosen to be -5 °C, or equivalently 2.5 in $\log(\dot{\epsilon})$. The yield stress data were then mapped into one diagram, Fig. 10a, and a set of equivalent stress-strain curves was also produced with matching yield stresses from experiments changing either loading rates or temperatures, Fig. 10b. The yield stresses (Fig. 10a) match very well, although the data

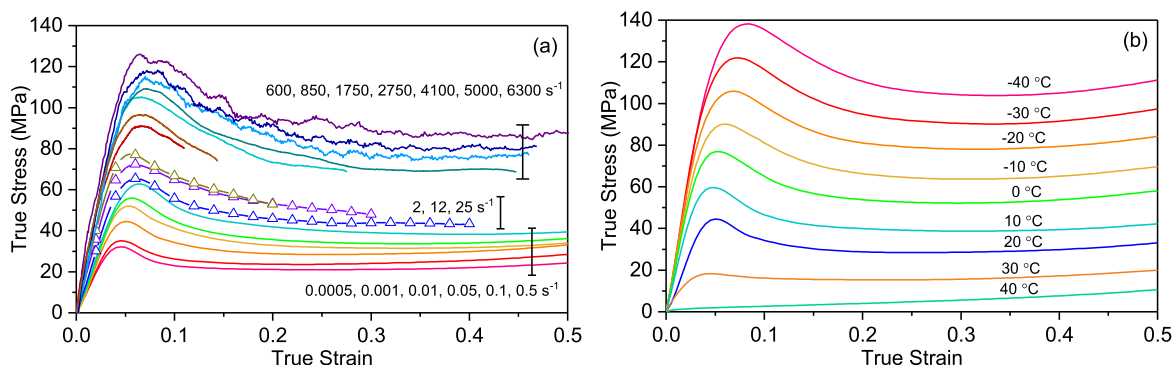


Fig. 7. Empirical strain-stress behaviour for epoxy at different rates (a) and temperatures (b).

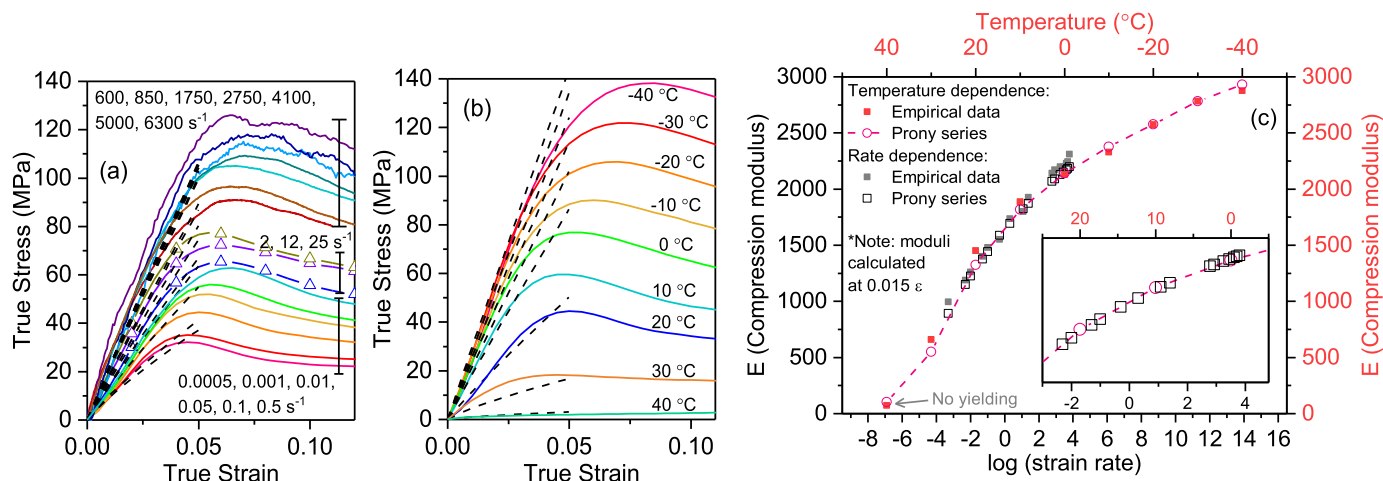


Fig. 8. Comparison of moduli between compression data and the generalized Maxwell model. (a) and (b) compare stress-strain curves from the experiments (coloured lines) and model (dashed lines) at different rates (a) and temperatures (b). (c) compares moduli extracted from the stress-strain curves (secant moduli at a strain of 0.015) to those calculated from the Maxwell model.

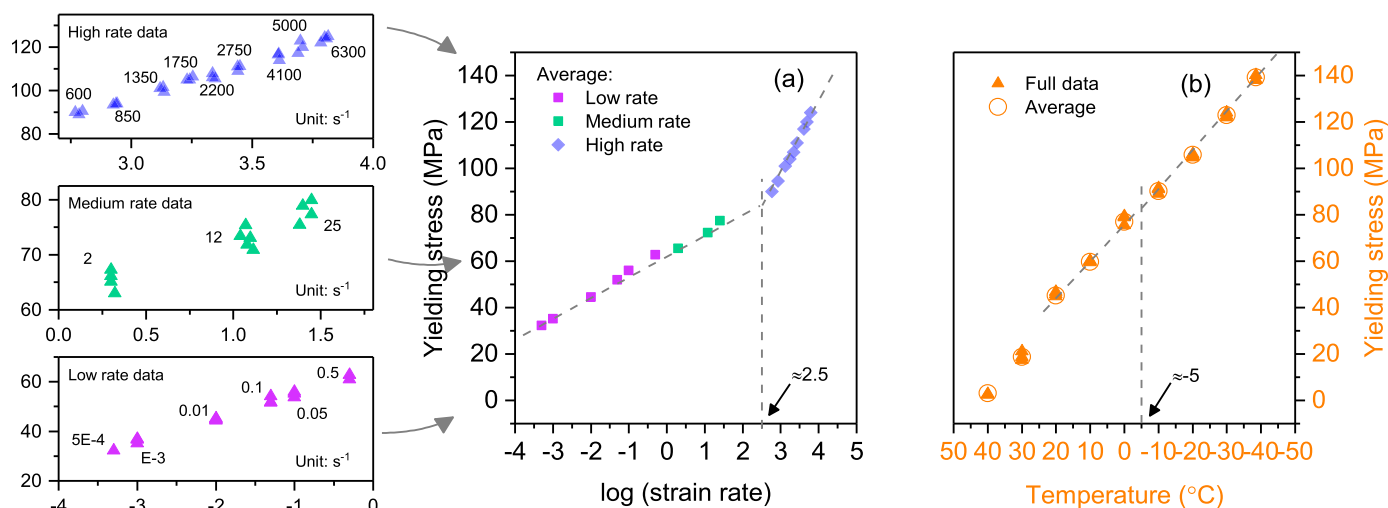


Fig. 9. Full yield stress data for epoxy: (a) at different rates and (b) at different temperatures.

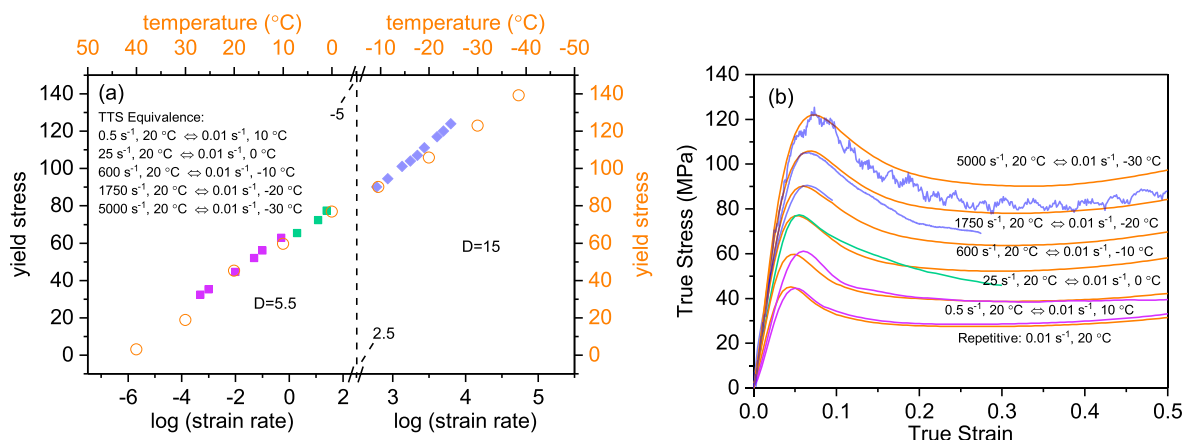


Fig. 10. (a) Application of time-temperature equivalence with $D = 5.5$ K per decade of strain rate for experiments at low-to-medium rates or above -5 °C; and $D = 15$ K per decade of strain rate for experiments at high rates or below -5 °C. (b) comparison of stress-strain curves from rate-and-temperature dependent experiments which have similar yield stress levels.

at high rates are slightly higher than the nominally equivalent data at low temperatures: it should be remembered that these data have been obtained using a mapping constant obtained from independently obtained DMA data. Comparing curves with matching yield stresses, (Fig. 10b), the stresses at larger strains are slightly lower in the high rate experiments, this is likely to be the result of adiabatic heating in these specimens. Whilst the use of a continuously variable D would give better matching, this simple approach gives a good understanding of the basic processes governing the behaviour, namely the shift of the β -transition to room temperature during high strain rate loading. The comparison of the stress-strain curves shows good agreement at small strains, but at larger strains the high strain rate data exhibit lower stresses than the equivalent low rate experiments because of the adiabatic heating effect [14]. Fig. 11 summarises a wider set of empirical data: yield stress and plateau stress and the drop between them. Here it is noted that the yield stress is affected by the glass and (at high rate) β relaxations, whilst the plateau appears to be affected only by the glass transition, combined with the adiabatic heating, see also [42,43].

4.3. Constitutive model

The uniaxial compression experiments were used to calibrate a parallel network model based on the three-network (TN) model, but without the large strain entropic network (C). The shear moduli for network A and network B are set to sum to the storage modulus from the DMA experiments ($G_{DMA} = \mu_A + \mu_B$). The values of μ_A and μ_B used are given in the SI; the appropriate distribution of network stiffness was determined as $\mu_A:\mu_B = 0.65:0.35$. The pressure-dependent parameter a is calculated by comparing yield stresses in uniaxial compressive and tensile experiments (Fig. SI-1, SI). Most of the remaining parameters were assigned by fitting to the empirical data, as described below. Some parameters, which have limited effect on the stress-strain curves under these conditions, were given assumed values: λ_L , $\hat{\tau}_B$, and m_B . The bulk modulus, k , which again has limited effect on these data, is an estimated value from the modulus [44]. A sensitivity analysis for these four parameters is given in the SI. The definition for all the parameter and the final values used are given in Table 1. The parameter calibration and model simulations were performed within software tools MCalibration® and PolymerFEM® [28,39].

The first step, shown in Fig. 12, was to fit the model to each of the rate-dependent stress-strain curves individually for the parameters that govern the low and medium strain behaviour. This was done assuming a constant temperature of 293 K, and also setting the reference temperature, $\theta_0 = 293$ K. This means that the parameters $\hat{\theta}$, and n do not affect the behaviour. The parameters that have negligible effect on the low strain behaviour ($\epsilon < 0.5$) were fixed as follows: $\lambda_A = 5$, $k = 3000$, $\hat{\tau}_B = 50$, $m_B = 8$.

Table 1

Material parameters used in the three-network model.

Symbol	Value	Description
Network-A		
μ_A	$0.65G'_{DMA}$ (MPa)	Shear modulus of network A
$\hat{\tau}_A$	25.5 MPa	Flow resistance of network A
m_A	15.7	Stress exponential of network A
Network-B		
μ_{B0}	$0.35G'_{DMA}$ (MPa)	Initial shear modulus of network B
μ_{Bf}	$\mu_{Bf}(\dot{\epsilon}, T)$ (MPa)	Final shear modulus of network B
β	16.5	Evolution rate of μ_B
$\hat{\tau}_B$	50 MPa	Flow resistance of Network B (assumed value)
m_B	8	Stress exponential of Network B (assumed value)
Thermal Coefficients		
θ_0	293 K	Thermal reference temperature
n	$n(T)$	Temperature exponent
$\hat{\theta}$	-100 K	Temperature factor (negative in compression)
Pressure Dependence		
a	0.26	Pressure dependence of flow
Large Strain Parameters (not fitted in this paper)		
λ_L	5	Locking stretch (assumed value)
k	3500 MPa	Bulk modulus (assumed value)

For high rate behaviour, the adiabatic heating option was employed: the heat capacity was measured from DSC experiments as $1180 \text{ J kg}^{-1} \text{ K}^{-1}$. The adiabatic heat conversion, often called the Taylor-Quinney Coefficient or beta-factor, was chosen through a comparison between the rate dependent and temperature dependent data. A value of 0.2 was eventually used: if a higher value was used, the required adjustments of μ_{Bf} either led to too much softening of the high rate stress-strain curves or too much hardening of the low rate curves; in order to enable these calculations values of $\hat{\theta} = -100$ and $n = 100$, which are the average values calibrated from temperature-dependent simulations were used. This remarkably low value for the Taylor-Quinney coefficient is consistent with observations made by Kendall and Siviour [45] that the observed mechanical behaviour does not require very large temperature rises in the specimen.

Eventually, then, this process gave a series of values of $\hat{\tau}_A$, m_A , β and μ_{Bf} as a function of strain rate. A similar approach to fitting the temperature dependent experimental data by considering each curve individually was also followed to give values of $\hat{\theta}$ and n . In practice, the strain rate and temperature-dependent fitting were performed synchronously, at the end of which values of $\hat{\theta} = -100$ K, $n(20^\circ \text{C}) = 100$ were used in the rate-dependent simulations and average parameters $\hat{\tau}_A = 25.5$ MPa, $m_A = 15.7$, $\beta = 16.5$ were used in the temperature-dependent simulations.

A second round of simulations, Fig. 13, was then performed using the average values of parameters in Fig. 12, apart from μ_{Bf} , and n , for which the relationships described in Fig. 11 were used. For the high rate

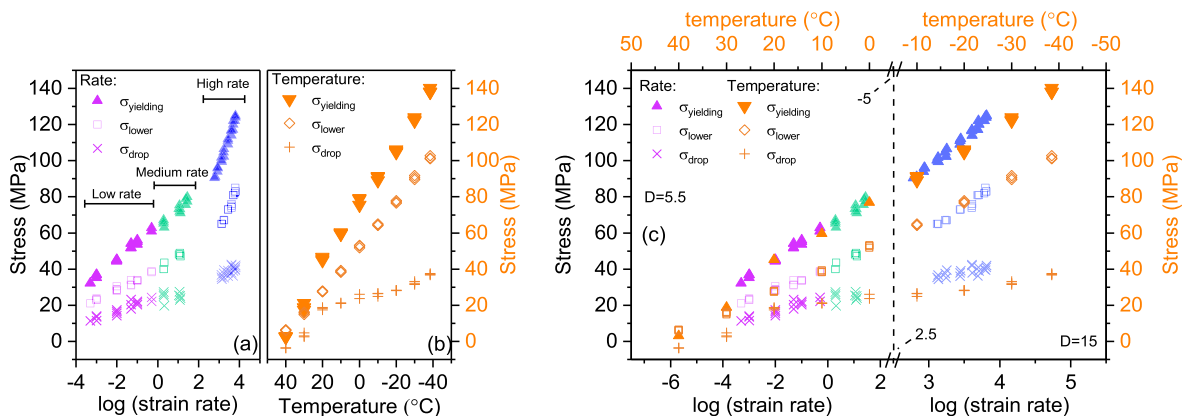


Fig. 11. (a) and (b) show the yield stress, plateau stress ($\epsilon = 0.35$) and stress drop (i.e. $\sigma_{\text{drop}} = \sigma_{\text{yielding}} - \sigma_{\text{lower}}$) for all experiments in which a strain of 0.35 was reached. (c) Application of time-temperature equivalence (Eq (1)) to empirical stress data using two independent variables: $D = 5.5$ and $D = 15$.

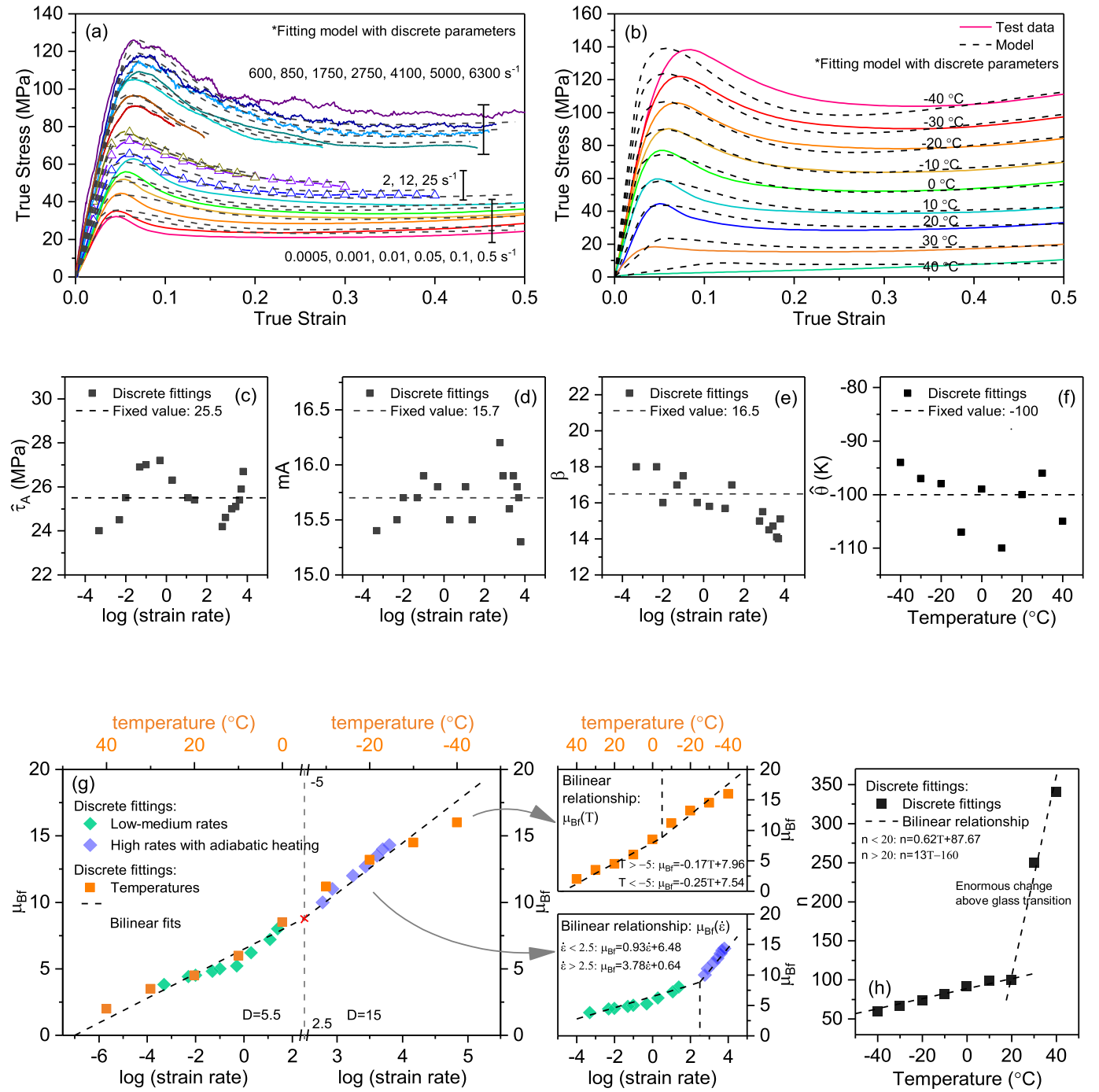


Fig. 12. Model using optimal parameters to calibrate the model against experiments at different rates, (a), and temperatures, (b). (c)–(f) show τ_A , m_A , β and $\hat{\theta}$ values obtained from these calibrations. (g) shows the rate and temperature dependence of μ_{Bf} , which has similarities to the dependences of experimentally determined moduli and yield stresses. This parameter was therefore assumed to follow bilinear relationships as shown. (h) shows the fitted values of n , again these appear to follow a bilinear relationship, but this time owing to the glass transition rather than the β -transition.

simulations ($\dot{\epsilon} > 600 \text{ s}^{-1}$), the temperature history was determined. Here, $n(20^\circ\text{C}) = 100$ was again used in these simulations instead of $n(T)$ in order to reduce the computation time; the effect of changing n to other realistic values was found to have a limited effect on the stress (about 2 MPa change at a strain of 0.5 for $n = 150$).

4.4. Model parameter sensitivity

The effect of the parameters on the stress-strain behaviour was

examined. First, the split of the measured shear modulus between μ_A and μ_{Bi} was investigated; Fig. 14 indicates that smaller μ_A (i.e. larger μ_{Bi}) gives a higher yield stress, in turn leading to a larger stress drop in the post-yield region. Fig. 15 presents the effect of changing τ_A , m_A , μ_{Bf} and β . Changing τ_A and m_A both scale the whole stress-strain curve, the latter having more effect at high strain rates. Larger values of μ_{Bf} affect the stress plateau at large strains, whilst β primarily dictates how quickly stress drops from yield to the large strain value. There are only two variables affecting the temperature-dependence, shown in Fig. 16. The

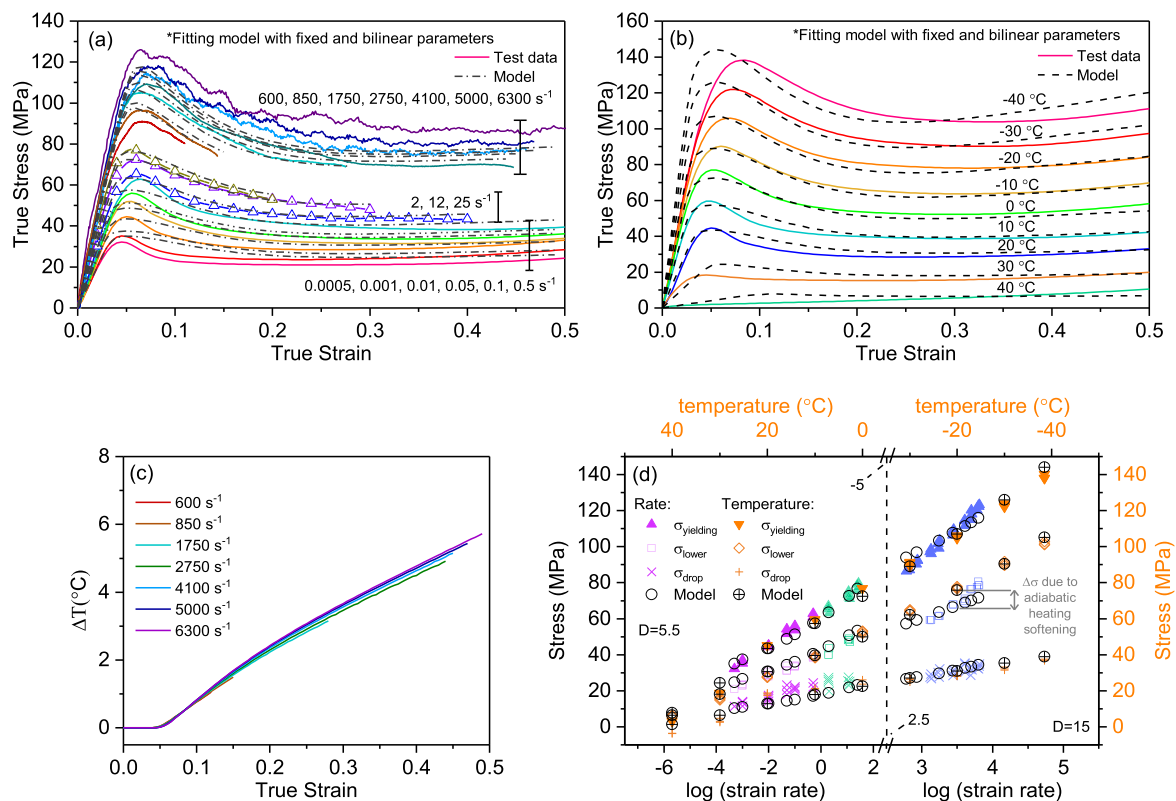


Fig. 13. Model using final parameters (Table 1) compared to experiments at different rates, (a), and temperatures, (b). Calibrations (a) and (b) were executed synchronously, with $\hat{\theta} = -100$ and $n(20^\circ\text{C}) = 100$ used in rate-dependent simulations. (c) describes the predicted temperature rise due to adiabatic heating in high-rate experiments when heat capacity and heat conversion were taken as $1180 \text{ J kg}^{-1} \text{ K}^{-1}$ and 0.2 respectively. (d) shows the comparison of yield stress, stress plateau and stress drop (softening) between experiments and models.

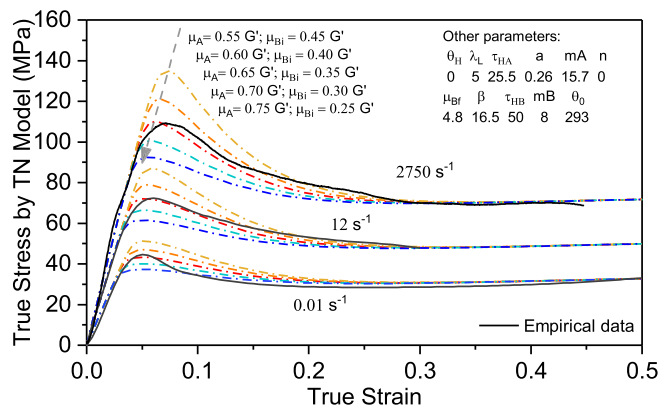


Fig. 14. Effect of the distribution of network-A and network-B shear moduli on ultimate stress-strain behaviour. The adiabatic heating effect was excluded in for the simulation at 2750 s^{-1} .

sensitivity to $\hat{\theta}$ is very small; whilst n has a large effect only at low temperatures. The sensitivities to other parameters with negligible influence on the stress-strain behaviour in the strain regime studies are shown in Fig. SI-3.

5. Discussion and conclusions

This paper presents results from uniaxial compression experiments on an epoxy resin over a wide range of strain rates, from quasi-static to

high rate, and temperatures (from -40 to 40°C). This was combined with a comprehensive study of thermal-mechanical properties performed on DSC and DMA apparatus. The principle of time-temperature superposition, for modulus data, and time-temperature equivalence, at larger strains was investigated. For the moduli, the equivalence parameter approach used in the literature was employed to map rate- and temperature-dependent experiments onto each other. Here, two values of the equivalence parameter were used, representing the different frequency dependencies of the glass and β transitions. This allowed interpretation of the observed 'bilinear' dependence on $\log(\text{strain rate})$. The mapping was not perfect at the higher strain rates (or lower temperatures); this departure may result from errors in the DMA data or the necessary extrapolation to very high rates, or the fact that a bilinear rather than continuously varying parameter was used; however the data shown demonstrate the power of this approach. For larger strain data, overlaid stress-strain curves in which the rate and temperature dependences of the moduli were matched showed good agreement at higher strains, apart from at the highest strain rates in which adiabatic heating in the high rate experiments plays a role in determining the behaviour. This was explored further in the modelling.

The data from DMA and DSC experiments showed both a primary glass transition and secondary transition at around 38°C ($\sim 311 \text{ K}$) and -18°C ($\sim 255 \text{ K}$) respectively, although the secondary transition was not easily observed in the storage moduli. Data from the DMA was used to produce a master curve from which a generalized Maxwell model was calibrated. Moduli show good agreement between the DMA data and rate-and-temperature dependent compression experiments. The bilinear behaviour of the yield stress has a change in gradient at around $\log(\dot{\epsilon}) = 2.5$.

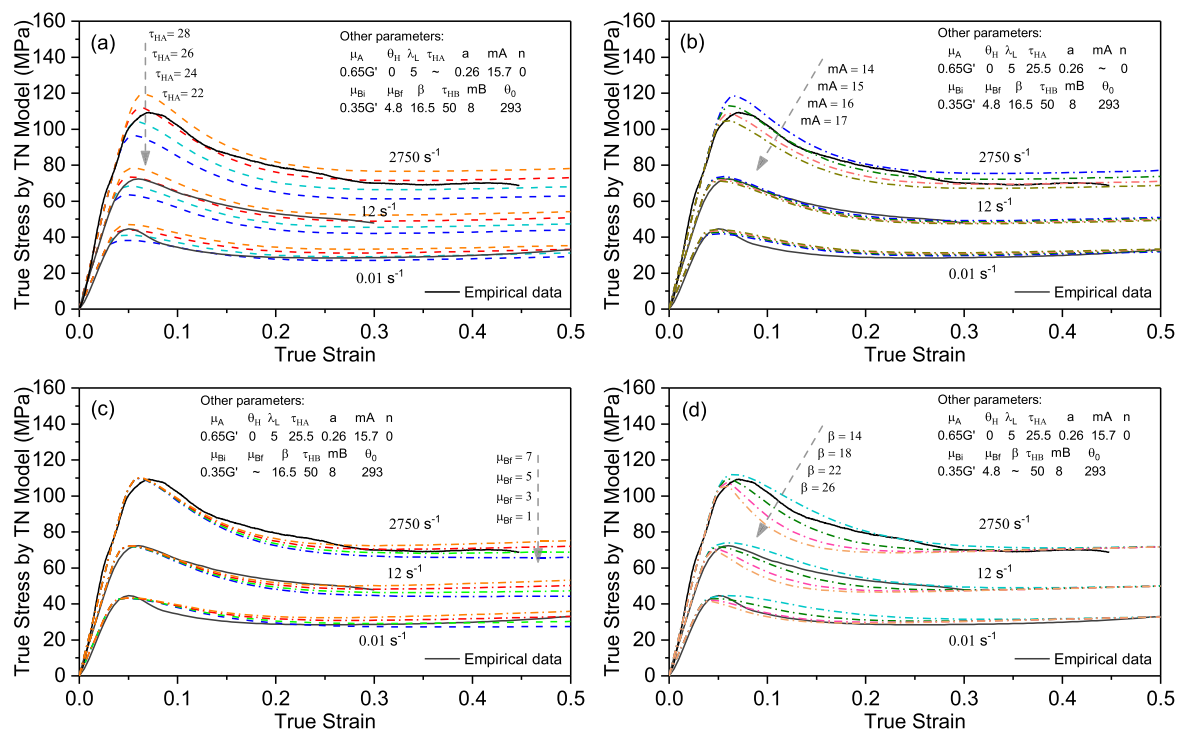


Fig. 15. Effect of $\hat{\tau}_A$, m_A , μ_{Bf} and β on ultimate stress-strain behaviour. The adiabatic heating effect was excluded for the simulation at 2750 s^{-1} .

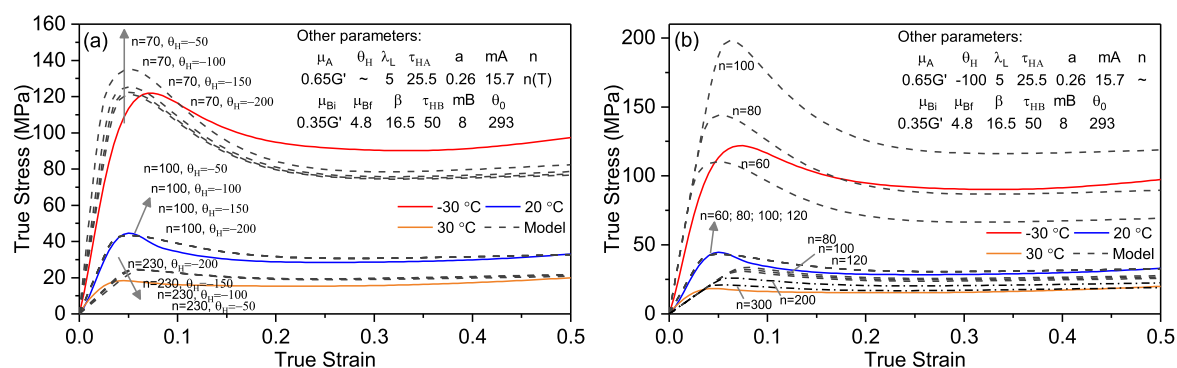


Fig. 16. Effect of $\hat{\theta}$ and n on ultimate stress-strain behaviour.

The three-network (TN) model for polymers was fit to the experimental data. This model shows excellent agreement with the experiments. Of particular interest was the application of adiabatic heating, for which it was found that a conversion of plastic work to heat (Taylor-Quinney factor) of 0.2 was required to obtain good fits to both the high strain rate and low temperature quasi-static results. This is consistent with observations in the literature about the temperature rises required to explain the high rate data, but would not have been known had the model been fitted to rate dependent data only: this shows the importance of a combined approach making use of time-temperature equivalence. In these models, the value of β was fixed, however, there is some evidence that β decreases at high strain rates, and this is explored further in Fig. SI-5. The parameter sensitivity for the model implementation was also discussed, it clarifies the effect of each of the parameters on global stress-strain behaviour.

This research provides an all-round study on an epoxy polymer, characterises time-temperature properties, implements an appropriate material model for compression experiments over a range of strain rates

and temperatures. It additionally provides a good database for both industrial and commercial use of this particular epoxy polymer.

Data availability

The raw/processed data to support this article can be found online from Mendeley Data: 'Experimental characterization and modelling of bisphenol-a type epoxy polymer in high strain rates and low temperatures', Mendeley Data, V2, <https://doi.org/10.17632/hy2vkn2v7z.2>.

CRediT authorship contribution statement

Huanming Chen: Conceptualization, Methodology, Validation, Formal analysis, Investigation, Software, Writing – original draft. **Pei-hao Song:** Investigation, Visualization. **Tom Commings & Aaron Graham:** Experiments. **Akash R. Trivedi:** Software. **Clive R. Siviour:** Resources, Conceptualization, Project administration, Supervision, Writing – review & editing.

Declaration of competing interest

The authors declare that they have no known competing financial interests or personal relationships that could have appeared to influence the work reported in this paper.

Acknowledgements

This material is based upon work supported by the Air Force Office of Scientific Research, Air Force Material Command, USAF under Award No. FA9550-15-1-0448. The funders had no involvement in study design, collection, analysis and interpretation of data, writing of the report or the decision to submit the article for publication. We thank Dr. Daohe Yuan, at Oxford University, for insight and expertise in polymer research and NMR-relative advice. We also would like to thank Dr Igor Dyson for technical support at Oxford University and, in particular, Nick Hawkins for invaluable support with the experiments on the DMA.

Appendix A. Supplementary data

Supplementary data to this article can be found online at <https://doi.org/10.1016/j.polymer.2022.124860>.

References

- [1] C.R. Siviour, S.M. Walley, W.G. Proud, J.E. Field, The high strain rate compressive behaviour of polycarbonate and polyvinylidene difluoride, *Polymer* 46 (2005) 12546–12555, <https://doi.org/10.1016/j.polymer.2005.10.109>.
- [2] S.M. Walley, J.E. Field, Strain rate sensitivity of polymers in compression from low to high rates, *DYMAT J* 1 (1994) 211–227, www.researchgate.net/publication/284674707.
- [3] M.J. Kendall, C.R. Siviour, Rate dependence of poly (vinyl chloride), the effects of plasticizer and time-temperature superposition, *Proc. R Soc. A Math Phys. Eng. Sci.* 470 (2014) 20140012, <https://doi.org/10.1098/rspa.2014.0012>.
- [4] W.D. Cook, A.E. Mayr, G.H. Edward, Yielding behaviour in model epoxy thermosets—II. Temperature dependence, *Polymer* 39 (1998) 3725–3733, [https://doi.org/10.1016/S0032-3861\(97\)10335-4](https://doi.org/10.1016/S0032-3861(97)10335-4).
- [5] E.N. Brown, P.J. Rae, G.T. Gray, The influence of temperature and strain rate on the tensile and compressive constitutive response of four fluoropolymers, *J. Phys. IV* 134 (2006) 935–940, <https://doi.org/10.1051/jp4:2006134143>.
- [6] C.R. Siviour, J.L. Jordan, High strain rate mechanics of polymers: a review, *J. Dyn. Behav. Mater.* 2 (2016) 15–32, <https://doi.org/10.1007/s40870-016-0052-8>.
- [7] J.L. Jordan, J.R. Foley, C.R. Siviour, Mechanical properties of Epon 826/DEA epoxy, *Mech. Time-Dependent Mater.* 12 (2008) 249–272, <https://doi.org/10.1007/s11043-008-9061-x>.
- [8] T. Gómez-del Río, J. Rodríguez, Compression yielding of epoxy: strain rate and temperature effect, *Mater. Des.* 35 (2012) 369–373, <https://doi.org/10.1016/j.matdes.2011.09.034>.
- [9] S. Tamrakar, R. Ganesh, S. Sockalingam, B.Z. Haque, J.W. Gillespie, Experimental investigation of strain rate and temperature dependent response of an epoxy resin undergoing large deformation, *J. Dyn. Behav. Mater.* 4 (2018) 114–128, <https://doi.org/10.1007/s40870-018-0144-8>.
- [10] Y. Tian, H. Zhang, J. Zhao, T. Li, B.-X. Bie, S.-N. Luo, et al., High strain rate compression of epoxy based nanocomposites, *Compos. Part A Appl. Sci. Manuf.* 90 (2016) 62–70, <https://doi.org/10.1016/j.compositesa.2016.06.008>.
- [11] J. Diani, P. Gilormini, J.S. Arrieta, Direct experimental evidence of time-temperature superposition at finite strain for an amorphous polymer network, *Polymer* 58 (2015) 107–112, <https://doi.org/10.1016/j.polymer.2014.12.045>.
- [12] D.M. Williamson, C.R. Siviour, W.G. Proud, S.J.P. Palmer, R. Govier, K. Ellis, et al., Temperature-time response of a polymer bonded explosive in compression (EDC37), *J. Phys. D Appl. Phys.* 41 (2008) 85404, <https://doi.org/10.1088/0022-3727/41/8/085404>.
- [13] J.L. Jordan, C.R. Siviour, J.R. Foley, E.N. Brown, Compressive properties of extruded polytetrafluoroethylene, *Polymer* 48 (2007) 4184–4195, <https://doi.org/10.1016/j.polymer.2007.05.038>.
- [14] M.J. Kendall, C.R. Siviour, Experimentally simulating adiabatic conditions: approximating high rate polymer behavior using low rate experiments with temperature profiles, *Polym. (United Kingdom)* 54 (2013) 5058–5063, <https://doi.org/10.1016/j.polymer.2013.06.049>.
- [15] C. Sorini, A. Chattopadhyay, R.K. Goldberg, Micromechanical modeling of the effects of adiabatic heating on the high strain rate deformation of polymer matrix composites, *Compos. Struct.* 215 (2019) 377–384, <https://doi.org/10.1016/j.compstruct.2019.02.016>.
- [16] Z. Pan, B. Sun, V.P.W. Shim, B. Gu, Transient heat generation and thermo-mechanical response of epoxy resin under adiabatic impact compressions, *Int. J. Heat Mass Tran.* 95 (2016) 874–889, <https://doi.org/10.1016/j.ijheatmasstransfer.2015.12.072>.
- [17] S. Tamrakar, R. Ganesh, S. Sockalingam, B.Z. Haque, J.W. Gillespie Jr., Strain rate-dependent large deformation inelastic behavior of an epoxy resin, *J. Compos. Mater.* 54 (2020) 71–87, <https://doi.org/10.1177/0021998319859054>.
- [18] J. Furmanski, C.M. Cady, E.N. Brown, Time-temperature equivalence and adiabatic heating at large strains in high density polyethylene and ultrahigh molecular weight polyethylene, *Polymer* 54 (2013) 381–390, <https://doi.org/10.1016/j.polymer.2012.11.010>.
- [19] E.N. Brown, R.B. Willms, G.T. Gray, P.J. Rae, C.M. Cady, K.S. Vecchio, et al., Influence of molecular conformation on the constitutive response of polyethylene: a comparison of HDPE, UHMWPE, and PEX, *Exp. Mech.* 47 (2007) 381–393, <https://doi.org/10.1007/s11340-007-9045-9>.
- [20] X. Chen, J. Lai, X. Chang, Y. Zhang, L. Zhang, C. Wang, Compressive mechanical properties of HTPB propellant at low temperatures and high strain rates, *Results Phys.* 7 (2017) 4079–4084, <https://doi.org/10.1016/j.rinp.2017.10.034>.
- [21] L. Yang, N. Wang, K. Xie, X. Sui, S. Li, Influence of strain rate on the compressive yield stress of CMDB propellant at low, intermediate and high strain rates, *Polym. Test.* 51 (2016) 49–57, <https://doi.org/10.1016/j.polymertesting.2016.02.007>.
- [22] J. Richeton, S. Ahzi, K.S. Vecchio, F.C. Jiang, R.R. Adharapurapu, Influence of temperature and strain rate on the mechanical behavior of three amorphous polymers: characterization and modeling of the compressive yield stress, *Int. J. Solid Struct.* 43 (2006) 2318–2335, <https://doi.org/10.1016/j.ijsolstr.2005.06.040>.
- [23] J. Richeton, S. Ahzi, L. Daridon, Thermodynamic investigation of yield-stress models for amorphous polymers, *Philos. Mag. A* 87 (2007) 3629–3643, <https://doi.org/10.1080/14786430701381162>.
- [24] A.D. Mulliken, M.C. Boyce, Mechanics of the rate-dependent elastic-plastic deformation of glassy polymers from low to high strain rates, *Int. J. Solid Struct.* 43 (2006) 1331–1356, <https://doi.org/10.1016/j.ijsolstr.2005.04.016>.
- [25] C. Sorini, A. Chattopadhyay, R.K. Goldberg, An improved plastically dilatant unified viscoplastic constitutive formulation for multiscale analysis of polymer matrix composites under high strain rate loading, *Compos. B Eng.* 184 (2020) 107669, <https://doi.org/10.1016/j.compositesb.2019.107669>.
- [26] H. Park, M. Cho, A multiscale framework for the elasto-plastic constitutive equations of crosslinked epoxy polymers considering the effects of temperature, strain rate, hydrostatic pressure, and crosslinking density, *J. Mech. Phys. Solid.* 142 (2020) 103962, <https://doi.org/10.1016/j.jmps.2020.103962>.
- [27] R. Unger, W. Exner, B. Arash, R. Rolfes, Non-linear viscoelasticity of epoxy resins: molecular simulation-based prediction and experimental validation, *Polymer* 180 (2019) 121722, <https://doi.org/10.1016/j.polymer.2019.121722>.
- [28] J.S. Bergstrom, J.E. Bischoff, An advanced thermomechanical constitutive model for UHMWPE, *Int. J. Struct. Chang. Solids* 2 (2010) 31–39, <https://journals.tdl.org/jscs/index.php/jscs/article/view/2350>.
- [29] F. Rueda, J.P. Torres, M. Machado, P.M. Frontini, J.L. Otegui, External pressure induced buckling collapse of high density polyethylene (HDPE) liners: FEM modeling and predictions, *Thin-Walled Struct.* 96 (2015) 56–63, <https://doi.org/10.1016/j.tws.2015.04.035>.
- [30] J.P. Torres, P.M. Frontini, M. Machado, Z. Major, Deformation and failure of semicrystalline polymers under dynamic tensile and biaxial impact loading, *Int. J. Impact Eng.* 98 (2016) 52–61, <https://doi.org/10.1016/j.ijimpeng.2016.08.004>.
- [31] M.L. Dreher, S. Nagaraja, J. Bergstrom, D. Hayman, Development of a flow evolution network model for the stress-strain behavior of poly (L-lactide), *J. Biomech. Eng.* 139 (2017), <https://doi.org/10.1115/1.4037071>.
- [32] S.S. Kulkarni, G.M. Mocko, A finite element simulation model of convective heat-assisted single-point incremental forming of thermoplastics, *Int. J. Adv. Manuf. Technol.* 111 (2020) 3305–3317, <https://doi.org/10.1007/s00170-020-06311-9>.
- [33] A. Shahin, I. Barsoum, M.D. Islam, Constitutive model calibration of the time and temperature-dependent behavior of high density polyethylene, *Polym. Test.* 91 (2020) 106800, <https://doi.org/10.1016/j.polymertesting.2020.106800>.
- [34] D.J. Quinn, J. Bergstrom, S. Chow, Development and experimental validation of an advanced nonlinear, rate-dependent constitutive model for polyether ether ketone (PEEK), *J. Med. Dev. Trans. ASME* 7 (2013), <https://doi.org/10.1115/1.4025831>.
- [35] I.B. Ozsoy, H. Choi, P. Joseph, G. Li, I. Luzinov, H. Zhao, Reinforced thermoplastic composites with interfacial microarchitectural anchoring: computational study, *Int. J. Solid Struct.* 112 (2017) 54–64, <https://doi.org/10.1016/j.ijsolstr.2017.02.021>.
- [36] J.S. Bergström, M.C. Boyce, Constitutive modeling of the time-dependent and cyclic loading of elastomers and application to soft biological tissues, *Mech. Mater.* 33 (2001) 523–530, [https://doi.org/10.1016/S0167-6636\(01\)00070-9](https://doi.org/10.1016/S0167-6636(01)00070-9).
- [37] Ministry of Craft Ltd, Safety Data Sheets for Ministry of Craft Resin, Minist Ltd, 2021, www.ministryofcraft.co.uk/. (Accessed 20 January 2022).
- [38] J.S. Bergstrom, *Mechanics of Solid Polymers: Theory and Computational Modeling*, William Andrew, 2015.
- [39] PolymerFEM. MCalibration and PolymerFEM User Manual, Polym LLC, 2020, www.polymerfem.com. (Accessed 2 February 2022).
- [40] M.L. Williams, R.F. Landel, J.D. Ferry, The temperature dependence of relaxation mechanisms in amorphous polymers and other glass-forming liquids, *J. Am. Chem. Soc.* 77 (1955) 3701–3707, <https://doi.org/10.1021/ja01619a008>.
- [41] I.M. Ward, D.W. Hadley, *An Introduction to the Mechanical Properties of Solid Polymers*, 1993.
- [42] L.C.A. Van Breemen, T.A.P. Engels, E.T.J. Klompen, D.J.A. Senden, L.E. Govaert, Rate- and temperature-dependent strain softening in solid polymers, *J. Polym. Sci., Part B: Polym. Phys.* 50 (2012) 1757–1771, <https://doi.org/10.1002/polb.23199>.
- [43] E.M. Arruda, M.C. Boyce, R. Jayachandran, Effects of strain rate, temperature and thermomechanical coupling on the finite strain deformation of glassy polymers,

- Mech. Mater. 19 (1995) 193–212, [https://doi.org/10.1016/0167-6636\(94\)00034-E](https://doi.org/10.1016/0167-6636(94)00034-E).
- [44] A.R. Plepys, R.J. Farris, Evolution of residual stresses in three-dimensionally constrained epoxy resins, *Polymer* 31 (1990), [https://doi.org/10.1016/0032-3861\(90\)90019-U](https://doi.org/10.1016/0032-3861(90)90019-U), 1932–6.
- [45] M.J. Kendall, C.R. Siviour, Experimentally simulating high-rate behaviour: rate and temperature effects in polycarbonate and PMMA, *Philos. Trans. R Soc. A Math Phys. Eng. Sci.* 372 (2014) 20130202, <https://doi.org/10.1098/rsta.2013.0202>.